

## Experimental analysis and modelling of c-crack propagation in silicon nitride ball bearing element under rolling contact fatigue



Mian Hammad Nazir\*, Zulfiqar Ahmad Khan, Adil Saeed

*NanoCorr, Energy and Modelling Research Group (NCEM), Bournemouth University Talbot Campus, Poole, Dorset, BH12 5BB, UK*

### ARTICLE INFO

#### Keywords:

Silicon nitride  
Ball bearing  
Rolling contact fatigue  
Finite element method  
c-crack propagation  
Monte-Carlo simulation

### ABSTRACT

A comprehensive model for predicting fatigue failure probability of surface c-shaped cracks in silicon nitride ball bearing elements under rolling contact fatigue (RCF) has been presented in this paper. Firstly, three-dimensional finite element analysis (FEA) is used to determine the stress intensity factors (SIFs) along the front of crack by using fracture mechanics approach. Then the propagation uncertainty of c-crack is evaluated by using surrogate models built upon highly accurate finite element modelling for equivalent stress intensity factors. Finally, the Monte Carlo Simulations combined with surrogate models are used to predict the failure probability of rolling ball bearing element. Simulation results reveal that it is possible to reduce the failure probability of ball bearing element up to 95% by reducing the maximum crack size and enhancing the fracture toughness of the ball material. The modelling results have been verified by experimental studies showing that the current predictions of c-crack fatigue failures were consistent with the experimental results. Fatigues crack initiation and propagation is a significant failure mechanism within ceramic ball bearing elements. It presents design and durability challenges for both manufacturers and users. A three-fold approach, to simulate fatigue propagation of c-shaped crack in rolling contact ceramic bearing element presented in this paper, is novel and will solve major durability issues within ceramic ball bearing elements subject to rolling contact fatigue.

### 1. Introduction

Silicon nitride ( $\text{Si}_3\text{N}_4$ ) compared to other ceramic materials show outstanding performance in rolling bearing applications under extreme loads, environments and speeds. Recent advancements in quality control of ceramic balls have reduced the probability of fatigue failures due to control of manufacturing defects. However, practically, it is very difficult to remove all defects such as micron and submicron level surface cracks, pores and inclusions in  $\text{Si}_3\text{N}_4$  bearing elements. Surface cracks in  $\text{Si}_3\text{N}_4$  balls are immensely hard to spot and can greatly reduce the rolling contact fatigue (RCF) performance of these balls [1].  $\text{Si}_3\text{N}_4$  ball bearing failures under rolling contact are majorly caused by ‘ring or c-cracks’ [2] which have curved shaped crack front. These cracks often result in spalling when subjected to rolling contact fatigue which ultimately results in the complete failure of rolling bearing elements. Although extensive experimental [3–8] and modelling work [9–14] has been published, it is still not completely clear that how the surface c-cracks influence rolling contact fatigue of  $\text{Si}_3\text{N}_4$  ball bearings.

Fatigue failure procedure can be divided in to two stages i.e. crack initiation and propagation. Fig. 1 shows an example of c-crack initiation and propagation during rolling contact bench testing. Propagation of

crack in a cracked body governs its fatigue life. The cracks propagate under continuous rolling contact fatigue conditions until they become large enough such that a bulk of material is broken off from the surface resulting in spalling [15]. The major problems are; (i) how to predict the conditions for the growth of c-crack under rolling contact fatigue and (ii) how to predict the speed and direction of crack growth. Till now, there is no adequate solution to the main problems.

Fatigue failure of ball bearings can be predicted by using various stochastic methods due to uncertain nature of system parameters. These parameters include (i) uncertain crack geometry, (ii) uncertain crack position, and (iii) uncertain applied loads. Traditional computational approaches require significant resources for example cost and time to simulate the reliability of the system due to uncertain parameters. Such limitations were overcome by various alternative computational methods such as FORM/SORM methods [16], the inverse reliability (IR) method [17], the inverse sampling (IS) method and the Monte Carlo Simulations (MCS) using response surface [18] etc. All these methods have their own advantages and disadvantages however MCS using response surface provides much accurate reliability results compared to other methods which is why it has been utilised in this paper. Similar studies on reliability predictions have been previously performed and

\* Corresponding author.

E-mail address: [hnazir@bournemouth.ac.uk](mailto:hnazir@bournemouth.ac.uk) (M.H. Nazir).

Nomenclature	
a	Semi major axis of c-crack in x direction
a'	Semi major axis of semi-elliptical contact path
b	Semi minor axis of c-crack in z-direction
b'	Semi minor axis of semi-elliptical contact path
E	Young's modulus
G	Strain energy release rate.
$G = \frac{1}{E}(K_I^2 + K_{II}^2) + \frac{(1-\nu)}{E}K_{III}^2$	
H	x-coordinate of crack at surface on x - z plane
K	z-Co ordinate of crack at surface on x - z plane
$K_{eq}$	Equivalent stress at the front of crack
$K_I$	Opening stress intensity factor
$K_{II}$	Sliding stress intensity factor
$K_{III}$	Tearing stress intensity factor
$K_{eq_{th}}$	Threshold value which allows crack growth (fatigue threshold)
P	Normal pressure
$p_0$	Maximum value of Hertzian pressure
R	Effective ball radius for a ball-to-ball interaction.
$R \equiv \left(\frac{1}{R_1} + \frac{1}{R_2}\right)^{-1}$	
R	Distance from crack tip where u, v, and w are measured
$U_r, V, w$	Crack face opening, sliding and shearing displacements
$X_d$	Elliptical contact patch x-coordinate
$Y_d$	Elliptical contact patch y-coordinate
b/a	Aspect ratio of c-crack
$\mu$	Friction coefficient
$\nu$	Poisson's ratio
$\rho$	Material density
N	Number of Monte Carlo simulation samples
$N_f$	Number of simulation samples that fail
$N_C$	Number of simulation samples that lie in the contact patch
$P_f$	Probability of failure
$X_D$	Lateral position of crack to contact patch centre
$\omega$	Crack orientation
G	Limit state function

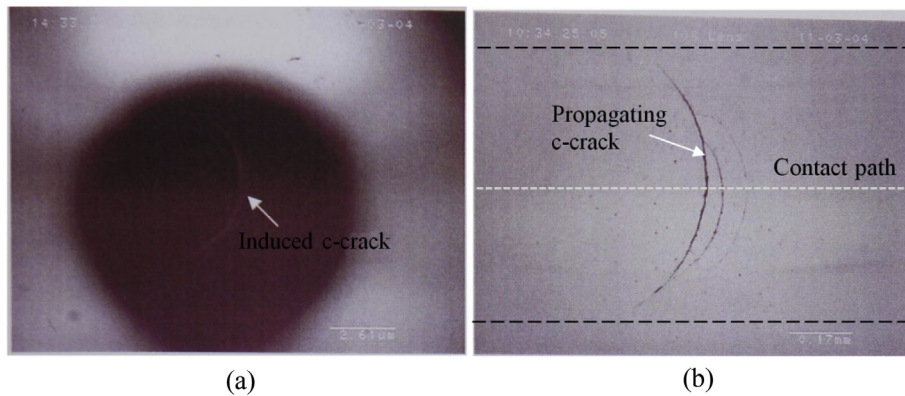


Fig. 1. (a) Light micrograph; dark field showing crack position in contact path (b) Light micrograph; secondary crack initiation and propagation [39].

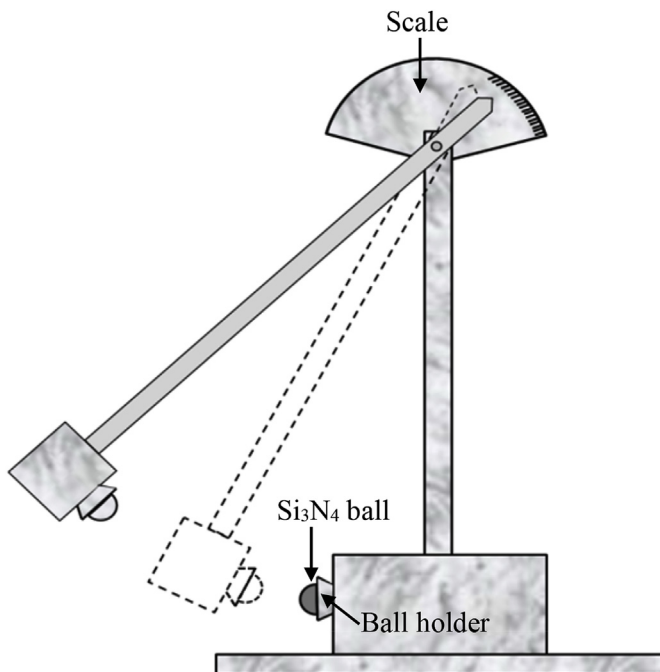


Fig. 2. Schematic of c-crack generating device (CGD).

presented [19–38].

A comprehensive model has been developed for uncertainty analysis of surface c-cracks in Si<sub>3</sub>N<sub>4</sub> ball bearings when subjected to RCF. During modelling; at first, finite element analysis (FEA) of c-shaped crack propagation and spall formation is performed. Then finite element modelling is used to build the surrogate models for equivalent stress intensity factors (SIFs) to evaluate uncertainty propagation. Next, the surrogate models combined with Monte Carlo Simulations (MCS) are utilised to estimate the failure probability of ball bearing element. Both Surrogate model and MCS are based on existing Sriram et al. approach [60]. Modelling results reveal that the failure probability can be decreased by reducing the maximum crack size and increasing the fatigue threshold (material toughness). Experiments were performed to analyse the influences of various c-crack parameters on RCF failure of Si<sub>3</sub>N<sub>4</sub> ball. Both the experimental results and the model predictions were compared to validate the reliability of the model.

## 2. Experiment

### 2.1. Materials

Si<sub>3</sub>N<sub>4</sub> balls were manufactured by hot iso-statically pressed (HIP) procedure. Average surface roughness ( $R_a$ ) of balls was 0.01 mm with average diameter as 12.7 mm. The Young's modulus, Poisson ratio and hardness of the balls were 310 GPa, 0.28 and 1637 Hv respectively. Surface profiles of ball bearing elements and characteristics of c-cracks

were examined by using light microscopy.

2.2. Sample preparation

An artificial surface c-crack was generated on each Si<sub>3</sub>N<sub>4</sub> ball with the help of a c-crack generating device (CGD) as shown in Fig. 2. The purpose of the artificially induced defect was to shorten the experimental time and observe failure mechanism due to the particular geometry of the induced defect. The swing angle (angle of impact), impact force and crack geometry were known. The arc length of the c-crack and angle were measured. The embedded area of the c-crack was also known. A special holder was designed and produced to clamp the ball into the holder for crack generation purposes. The load (in kg) for generating cracks and geometry was known.

2.3. Test equipment

The RCF tests were performed by using TE-92 Rotary Tribometer

[3]. This apparatus is capable of accurately simulating rolling contact under precise contact loads. The upper Si<sub>3</sub>N<sub>4</sub> ball with an artificially induced c-crack is mounted to a drive shaft via a collet. This ball makes a contact with the lower three steel balls. This whole setup is immersed in lubricant oil which has a kinematic viscosity of 25 cSt at 40° C. The setup is shown in Fig. 3 (a). The speed of Tribometer was set as 3000 rpm/min.

The position of ball is very important as c-crack orientation is critical in the contact path and has direct influence on the fatigue life of the ball. To study the failure mechanisms driven by a particular c-crack in the Si<sub>3</sub>N<sub>4</sub> ball surface, locating the c-crack into the contact path is vital. Once the c-crack is located in the contact path, its orientation is central to failure mechanisms. The normal contact pressure *p* dependent on applied radial load (shaft load) *L* and contact angle  $\psi$  ( $= 36^\circ$ ) is formulised as,

$$p = \frac{L}{3 \cos \psi} \tag{1}$$

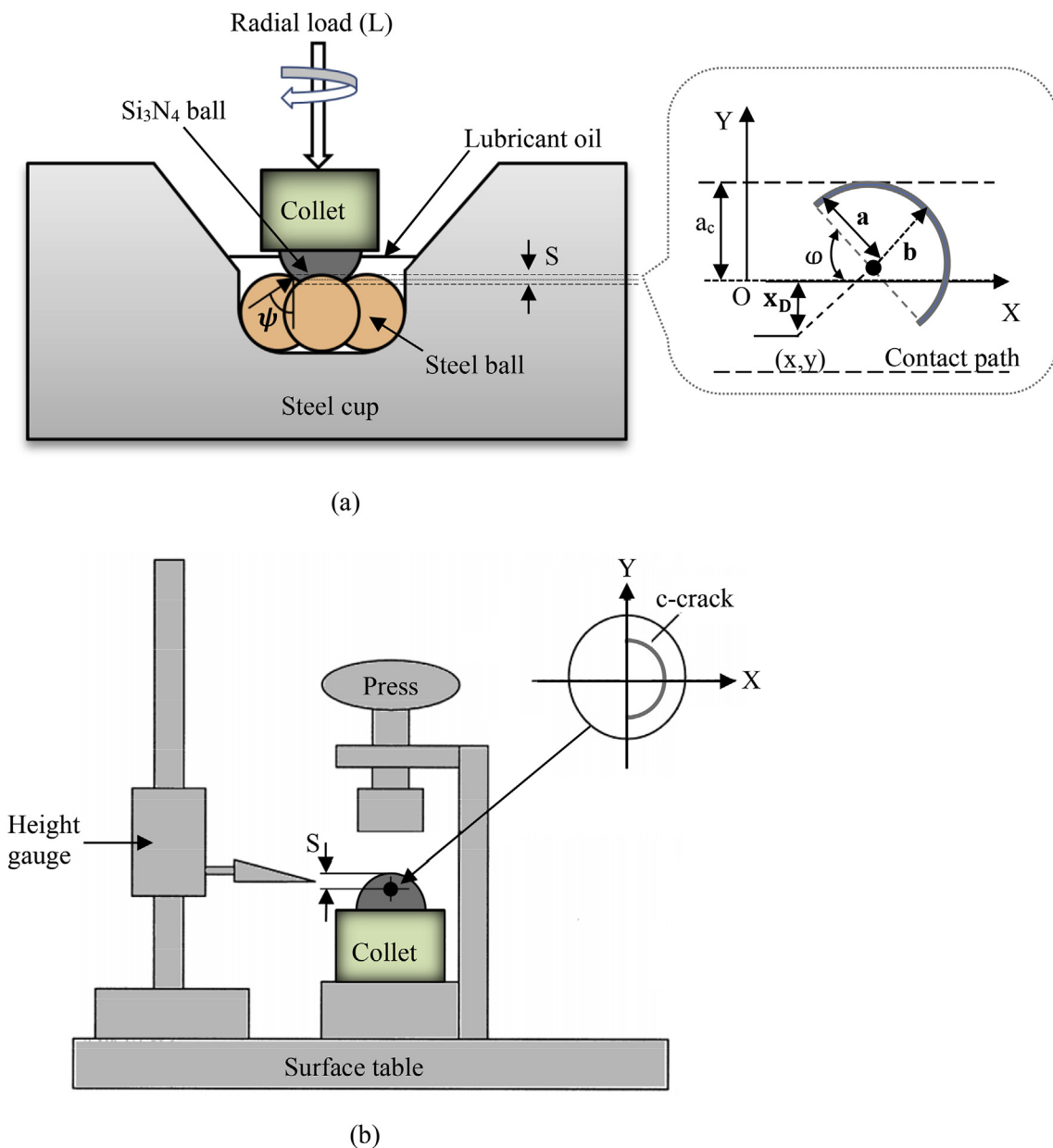


Fig. 3. Schematic showing: (a) a setup with an upper Si<sub>3</sub>N<sub>4</sub> ball in contact with the lower three steel balls and (b) a method for locating and offsetting the c-crack on specific position by using height gauge.

**Table 1**  
RCF tested scenarios with different c-crack positions [12].

	$\omega = 0^\circ$	$\omega = 45^\circ$	$\omega = 90^\circ$
$x_D = 0$			
$x_D = 0.5 a_c$			
$x_D = a_c$			

The maximum Hertzian contact pressure  $p_0$  and contact radius  $a_c$  can be evaluated by using [40],

$$p_0 = \left( \frac{6pE^{*2}}{\psi^3 R^3} \left[ \left( \frac{1-\nu_1^2}{E_1} + \frac{1-\nu_2^2}{E_2} \right)^{-1} \right]^2 \right)^{\frac{1}{3}} \quad (2)$$

$$a_c = \left( \frac{3P}{4E^*} \left( \frac{1}{R_1} + \frac{1}{R_2} \right)^{-1} \right)^{\frac{1}{3}} \quad (3)$$

where  $E_{1,2}$ ,  $\nu_{1,2}$  and  $R_{1,2}$  are the Young's modulus, Poisson's ratios and radii of the  $\text{Si}_3\text{N}_4$  ball and steel balls respectively ('1' is for  $\text{Si}_3\text{N}_4$  ball

and '2' is for steel balls). The random position of c-crack can exist at any position on  $\text{Si}_3\text{N}_4$  ball surface when both upper and lower balls come in contact. Therefore the following relationship could be utilised to calculate the probability of induced c-crack being in contact area [41].

$$\rho = \frac{a_c \sin \psi}{R_1} \quad (4)$$

As  $R_1 = 6.35$  mm,  $a_c = 0.21$  mm and  $\psi = 36^\circ$  therefore  $\rho = 0.02$ . From this result it can be seen that the c-crack probability to exist in the contact area is just 2%. Therefore, the crack positioning into the contact path is important. The upper ball must be positioned such that the

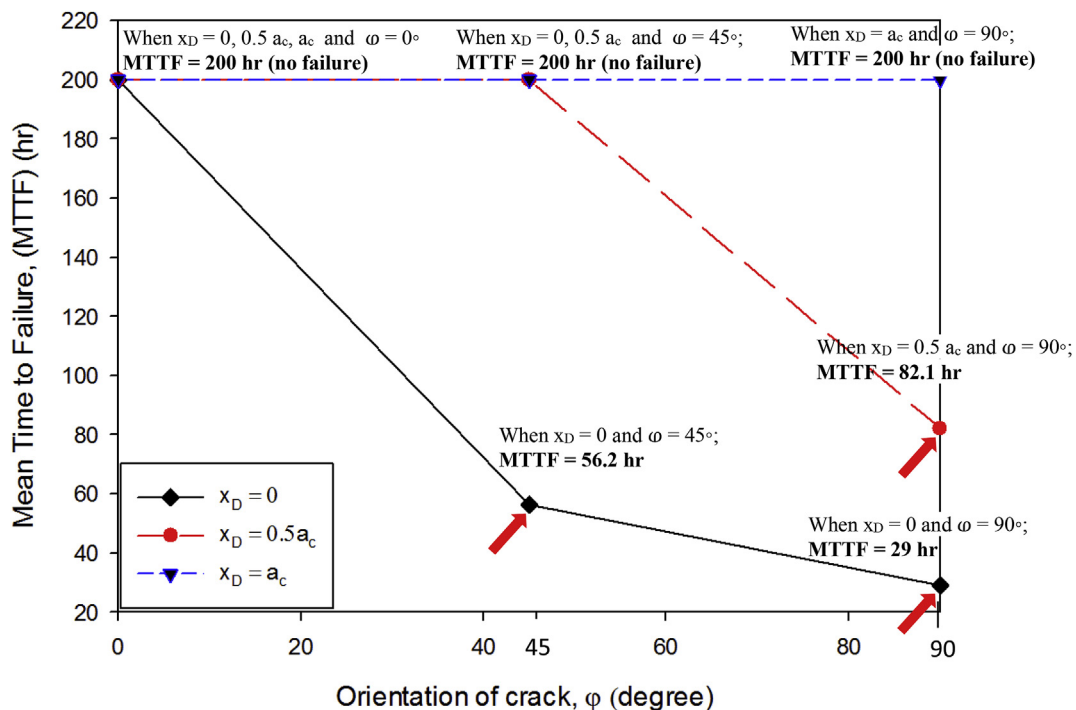


**Fig. 4.** RCF test results at various crack positions as a function of two parameters:  $\omega$  and  $x_D$ .

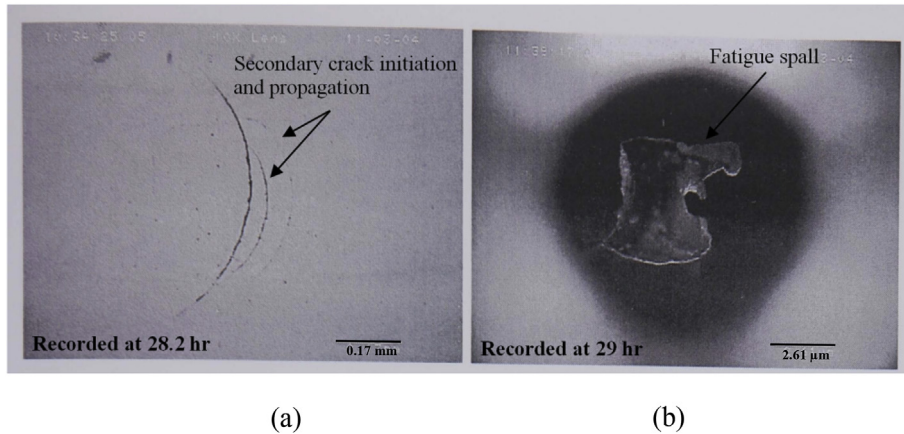


Fig. 5. The light micrographs of a propagating c-crack under RCF loading for the case:  $x_D = 0$  and  $\omega = 90^\circ$  recorded at (a) 28.2 h (b) 29 h.

induced c-crack remains in the contact path. This position is calculated as,

$$S = R_1 - (R_1 - \cos \psi) \tag{5}$$

Where S ( $S = 1.17$  mm) is the centre of the contact path from tip of ball surface as held in the collet. Fig. 3 (a) shows a schematic of the contact path offsetting from the tip of the ball surface. Positioning of the c-crack into 0.21 mm contact path is sensitive. The c-crack is observed and positioned under the optical microscope. The position is marked. The ball is then positioned into a manipulator held in the collet over a surface plate as shown in Fig. 3 (b) and the height of the ball surface is determined by using a height gauge. The c-crack is then offset by  $S = 1.17$  mm carefully without disturbing the required position of the c-crack into the contact path. After accurate positioning of the c-crack into the contact path the ball is then pressed into the collet using a press.

2.4. Test procedure

During this work two RCF studies were performed; first RCF study was performed by using various crack positions as shown in Table 1. The crack position is described by using two parameters. One is  $\omega$

(along the columns), which presents the orientation of crack and the second is  $x_D$  (along the rows), which is the normalised lateral position of crack front relative to the centre of contact path. These two positional parameters are clearly illustrated in Fig. 3 (a). There could be unlimited possible crack positions, however only few important positions are discussed in the present RCF study. The maximum contact pressure  $p_0$  for all the positions in Table 1 was constant  $6.23 \pm 0.5$  GPa.

The second RCF study was performed by using various geometrical parameters of c-crack such as crack semi major axis a and crack semi minor axis b as illustrated in Fig. 3 (a). Crack geometry also plays an important role in fatigue failure of  $Si_3N_4$  ball. The crack lengths: semi major and minor axis a and b respectively are selected as near as possible.

2.5. Experimental observations

2.5.1. Effect of crack position on RCF ( $x_D, \omega$ )

Fig. 4 shows the RCF test results at various crack positions. The RCF performance is directly influenced by two parameters:  $\omega$  and  $x_D$  for a given lubricant and contact load.

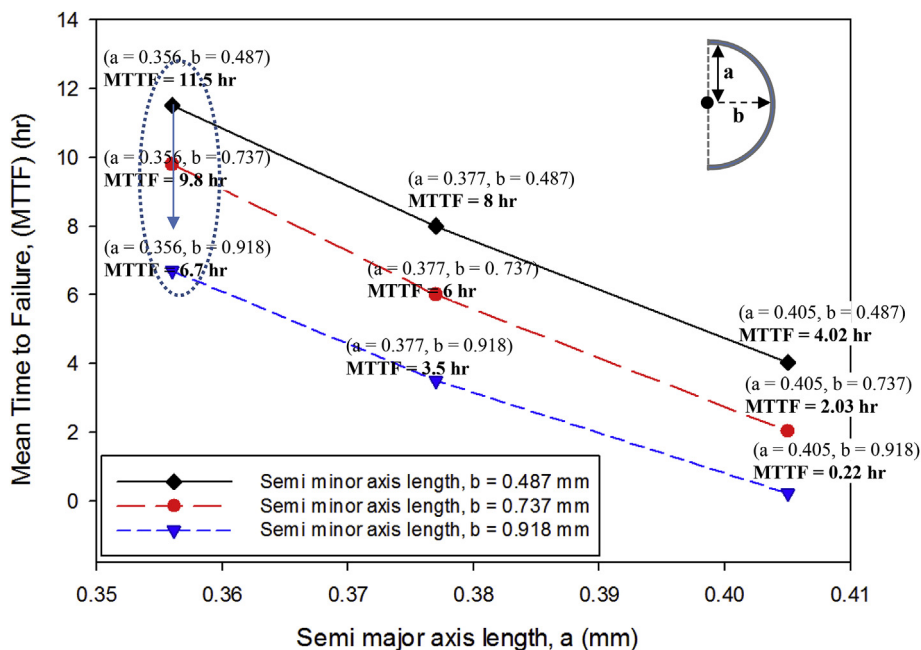


Fig. 6. RCF test results 9 typical geometries as a function of two parameters: a and b.

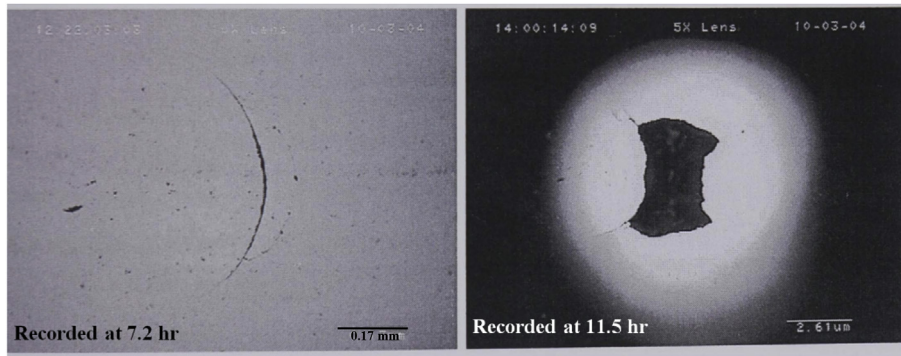


Fig. 7. The light micrographs of a propagating c-crack under RCF loading for the case: ( $a = 0.356$ ,  $b = 0.487$ ) recorded at 7.2 h and 11.5 h.

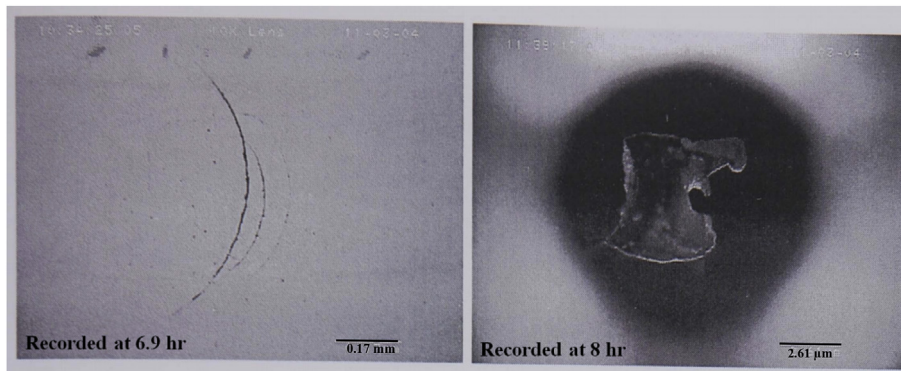


Fig. 8. The light micrographs of a propagating c-crack under RCF loading for the case: ( $a = 0.377$ ,  $b = 0.487$ ) recorded at 6.9 h and 8 h.

It can be seen in Fig. 4 that mean time to failure (MTTF) decreases with the increase in  $\omega$ . For the case (shown by black trend in Fig. 4) when  $x_D = 0$  and  $\omega = 90^\circ$ ,  $\omega = 45^\circ$  and  $\omega = 0^\circ$  the MTTFs are 29 h ( $1.723 \times 10^7$  stress cycles), 56.2 h ( $3.635 \times 10^7$  stress cycles) and 200 h ( $2.268 \times 10^8$  stress cycles and suspended with no failure) respectively.

For the case (shown by red trend) when  $x_D = 0.5 a_c$  and  $\omega = 90^\circ$ ,  $\omega = 45^\circ$  and  $\omega = 0^\circ$  the MTTFs are 82.1 h, 200 h and 200 h (suspended with no failure) respectively. For the case (shown by blue trend) when  $x_D = a_c$  and  $\omega = 90^\circ$ ,  $\omega = 45^\circ$  and  $\omega = 0^\circ$  all the MTTFs are 200 h meaning that no fatigue failures happened at all.

The test results of 9 crack positions clearly reveal that the fatigue failures were observed only at three positions which are indicated with red arrows in Fig. 4. The reason for distinct MTTF of various crack positions is that each corresponding position has different SIF values, which decide the behaviour and rate of crack propagation [3,8]. Large SIF value accounts for large propagation rate therefore lower MTTF and vice versa. This indicates that both SIF and MTTF are inversely related. For black trend ( $x_D = 0$ ), the SIF  $K_I$  for  $\omega = 90^\circ$  is largest corresponding to lowest MTTF (29 h) and the SIF  $K_I$  for  $\omega = 0^\circ$  is smallest corresponding to largest MTTF (200 h). Therefore due to distinct SIF  $K_I$  values the MTTF for three failed positions is different.

The light micrographs of a propagating c-crack under RCF loading for the case:  $x_D = 0$  and  $\omega = 90^\circ$  is shown in Fig. 5. Fig. 5 (a) was recorded at 28.2 h which showed the secondary crack initiation and propagation. The specimen failed into a fatigue spall after next 40 min. The fatigue spall is shown in Fig. 5 (b) using dark field in the light micrograph.

2.5.2. Effect of crack geometry on RCF ( $a$ ,  $b$ )

Fatigue life performances of the rolling contact bearing elements are influenced by the induced c-crack geometry as shown in Fig. 6. The test results of 9 typical geometries reveal that all the geometries resulted in fatigue failure. All these geometries had the same crack position:  $x_D = 0$

and  $\omega = 90^\circ$ . The linearly decreasing trends of MTTFs is seen with increasing semi major axis  $a$  of the c-crack while keeping semi major axis  $b$  constant. For example for the case when  $b$  is kept constant i.e.  $b = 0.487$  mm (shown by black trend), the MTTF reduces linearly by 65% from 11.5 h to 8 h and then to 4.02 h with increasing  $a$  from 0.356 mm to 0.377 mm and then to 0.405 mm respectively. Likewise for constant  $b = 0.737$  mm (red trend) and constant  $b = 0.918$  mm (blue

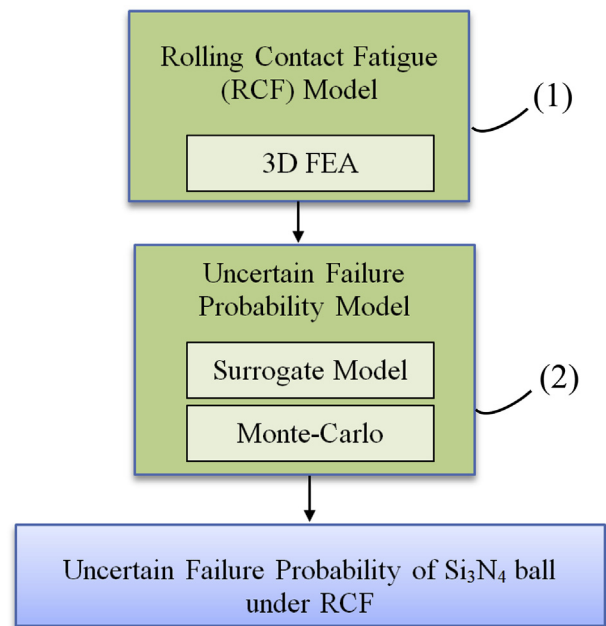


Fig. 9. The contents of modelling section addressing two main step-by-step topics to simulate the uncertain crack propagation method.

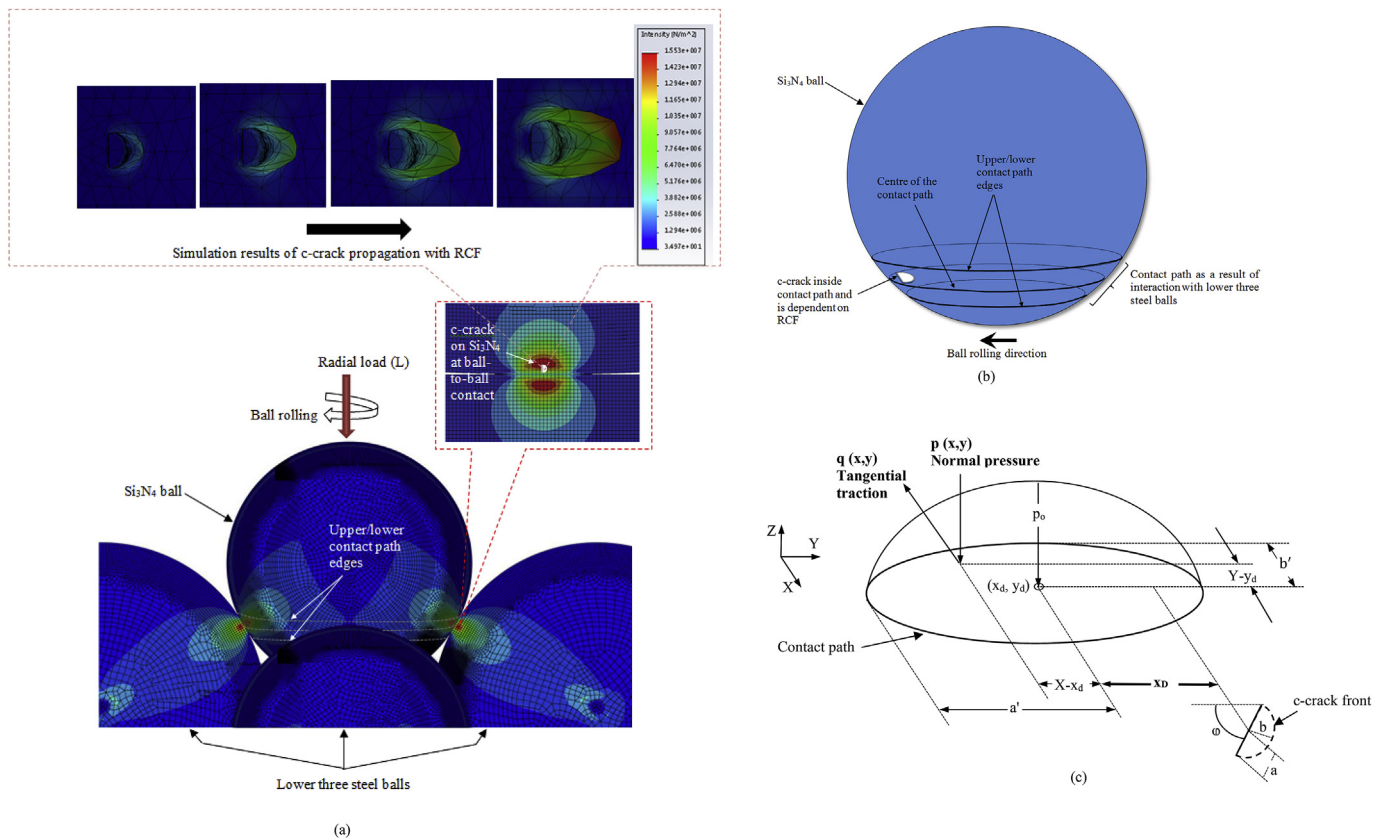


Fig. 10. (a) Loading configuration under ball-to-ball rolling with an incipient propagating c-crack located on ball surface (b) The upper Si<sub>3</sub>N<sub>4</sub> ball containing c-crack inside the contact path (c) Schematic of elliptical contact path containing c-crack inside the contact path in addition to figure showing various RCF parameters.

trend), 79% and 96% decrease in MTTFs are observed respectively with increasing a. The reason for decreasing MTTFs is the increase in the SIF values with increasing geometrical parameter a [8].

Similar behaviour showing decrease in MTTFs is observed when b is increased while a is kept constant for example in Fig. 6 the data points of all trends under dotted circle show decreasing behaviour of MTTFs (indicated by decreasing arrow) with increase in b while keeping a constant.

Therefore it can be seen from Fig. 6 that the worst fatigue performance (MTTF = 0.22 h) is shown by geometry which has the largest lengths of both a and b i.e. (a = 0.405, b = 0.918) while comparatively smallest geometry (a = 0.356, b = 0.487) showed the best fatigue performance (MTTF = 11.5 h) amongst all the 9 geometries.

Fig. 7 shows a light micrograph for crack geometry: (a = 0.356, b = 0.487). The image on the left was recorded at 7.2 h of test time. The secondary crack initiation and propagation in the contact path led to a mixed failure mechanism of delamination and fatigue spall at 11.5 h as shown in image on right. For another crack geometry (a = 0.377, b = 0.487) shown in Fig. 8, which has larger value of semi major axis a, the secondary crack propagation and fatigue spall are recorded at much reduced MTTFs of 6.9 h and 8 h respectively.

### 3. Modelling

The contents of modelling section, shown in Fig. 9, address two main step-by-step topics to simulate the overall stochastic RCF crack propagation method as: (1) development of the 3D finite element model for the c-crack fracture propagation and spall formation under RCF and (2) the development of surrogate models combined with Monte Carlo simulations (MCS) to evaluate uncertain crack propagation and failure probability predictions.

#### 3.1. Rolling contact fatigue (RCF) model

##### 3.1.1. Loading analysis

Loading configuration under ball-to-ball rolling with an incipient propagating c-crack located on upper Si<sub>3</sub>N<sub>4</sub> ball is shown in Fig. 10 (a). The upper Si<sub>3</sub>N<sub>4</sub> ball containing c-crack inside the contact path dependent on RCF is shown in Fig. 10 (b). The presence of c-crack with positional parameters (ω, x<sub>p</sub>) and geometrical parameters (a, b) result in higher crack tip loading under rolling contact load, for the same maximum Hertzian contact pressure p<sub>0</sub> compared to the ‘no crack’ case [13].

The normal contact pressure p(x, y) and the tangential traction q(x, y) of a moving Hertzian surface load is used to simulate the rolling contact load. Both p(x, y) and q(x,y) are shown in Fig. 10 (c) and are calculated as [42]:

$$p(x, y) = p_0 \sqrt{1 - \left[ \frac{(x - x_d)^2}{a'^2} + \frac{(y - y_d)^2}{b'^2} \right]} \quad (6)$$

$$q(x, y) = \mu p(x, y) \quad (7)$$

where p<sub>0</sub> represents the maximum Hertzian contact pressure, x<sub>d</sub> and y<sub>d</sub> represent distances to load centre from the global coordinate system, a' and b' are the semi-major and semi-minor axis of the elliptical contact path respectively (see Fig. 10 (c)), and μ in eq. (7) represents the coefficient of friction of a moving load. Here full-slip ball-to-ball contact is assumed during the movement. For cases when μ < 0 and μ > 0, the c-crack is run over by contact path from left-to-right and from right-to-left respectively. It is assumed that μ has a range in between 0.04 to 0.10 because of the elastohydrodynamic (EHD) lubrication [43]. EHD is a type of hydrodynamic lubrication (HL) in which significant elastic deformation of the surfaces takes place and it considerably results in asymmetric pressure profile as opposed to the symmetric Hertzian

pressure profile  $p_o$  [44]. Here RCF modelling assumes the Hertzian pressure profile to be symmetric neglecting elastic deformation during rolling contact. As the c-crack is run over by contact path from right-to-left ( $\mu > 0$ ) in Fig. 10 (c), the front of crack encounters a transition from compression to tensile stress repeatedly for every cycle.

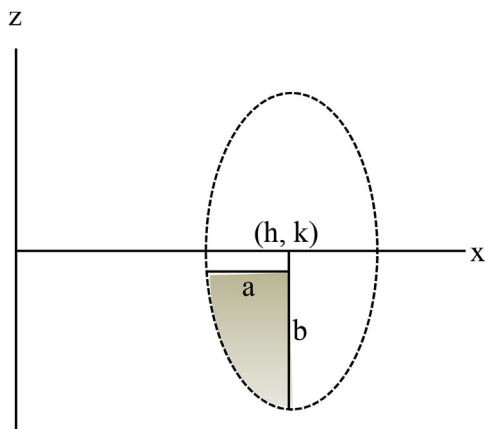
### 3.1.2. c-Crack geometry

The c-crack geometry plays the vital role in the fracture mechanics study and will be carefully analysed herein. In this research, c-crack geometry has been modelled as a partial cone by using the equations of an offset cylinder which has restricted dimensions for inequalities. This means that the c-crack's shape is a quarter ellipse which uses the cylindrical coordinates as shown in Fig. 11 (a) [13]. The height coordinate  $z$  which is the function of other geometrical parameters is given as,

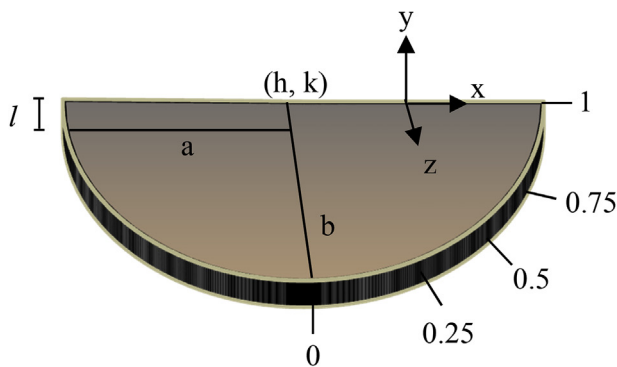
$$z = \frac{1}{ab} \sqrt{a^2 - (\sqrt{x^2 + y^2} - h)^2} + k - l \cos \phi \tag{8}$$

where

$$-\frac{1}{2}\phi_{\text{range}} \leq \tan^{-1}\left(\frac{y}{x}\right) \leq \frac{1}{2}\phi_{\text{range}} \tag{9}$$



(a)



(b)

Fig. 11. (a) The shape of c-crack which is a quarter ellipse and utilises the cylindrical coordinates (b) The 3D c-crack with position along the crack front from 0 (crack centre) to 1 (crack surface).

$$h - a \leq \sqrt{x^2 + y^2} \leq \frac{1}{2} \sec\left(\tan^{-1}\left(\frac{y}{x}\right)\right) \times \left[ \frac{1}{h - a} - \sqrt{2} \sin\left(\frac{1}{2}\phi_{\text{range}}\right) + (h - a) \right] \tag{10}$$

Where  $a$  and  $b$  are the semi major and semi minor axis of c-crack on the  $x$  and  $z$  axis respectively,  $h$  and  $k$  represent the  $x$  and  $z$  coordinates of the center of the quarter ellipse, respectively (see in Fig. 11 (a)),  $l$  is the depth of the c-crack and  $\phi$  is the orientation of c-crack (see in Fig. 10 (c)). The corresponding rendered 3D c-crack from Fig. 11 (a) with notation for the SIF plots is show in Fig. 11 (b). The position along the 3D c-crack front in Fig. 11 (b) is indicated from 0 to 1 with 0 representing the crack centre while 1 representing the crack surface.

### 3.1.3. Mixed mode stress intensity factor (SIFs) at c-crack tip due to RCF

The SIF calculation at the c-crack tip is a bit complicated process as it is a function of crack geometrical ( $a$  and  $b$ ), crack positional ( $x_D$  and  $\phi$ ), loading ( $p_o$ ) and material properties parameters. Here, the c-crack tip opening displacement (CTOD) method is used to calculate the SIFs [45]. Following generic equations have been utilised to obtain the values of three SIF modes ( $K_I$ ,  $K_{II}$  and  $K_{III}$ ) along the c-crack front due to RCF [13].

$$K_I = \frac{E}{4(1 - \nu^2)} \sqrt{\frac{2\pi}{r}} (u_1 - u_2) \tag{11}$$

$$K_{II} = \frac{E}{4(1 - \nu^2)} \sqrt{\frac{2\pi}{r}} (v_1 - v_2) \tag{12}$$

$$K_{III} = \frac{E}{4(1 - \nu^2)} \sqrt{\frac{2\pi}{r}} (w_1 - w_2) \tag{13}$$

where  $E$  and  $\nu$  represent the Young's modulus and Poisson's ratio respectively. The symbol  $u$  represents displacement perpendicular to face of c-crack,  $v$  represents displacement in the direction perpendicular to the crack tip,  $w$  represents the tangential line touching the crack tip and  $r$  represents length between crack tip and the point from where  $u$ ,  $v$  and  $w$  are measured. '1' and '2' are the points in time at which corresponding  $u$ ,  $v$  and  $w$  displacement components are evaluated. Fig. 12 (a) shows the coordinate system for the crack-tip opening displacement (CTOD).

In order to calculate the combined role of all three crack displacement modes ( $K_I$ ,  $K_{II}$  and  $K_{III}$ ) in the fatigue threshold  $K_{eq}$ , the equivalent mode-mix SIF  $K_{eq}$  is given as [46],

$$K_{eq} = \sqrt{EG} = \sqrt{E \left[ \frac{1}{E} (K_I^2 + K_{II}^2) + \frac{2(1-\nu)}{E} K_{III}^2 \right]} \tag{14}$$

The above equation for three-mode-dependent crack displacements  $K_{eq}$  utilises the fundamental fracture mechanics concept of strain energy release rate,  $G$  [46]. Where, the highest value of  $K_{eq}$  along the crack front is vital for figuring out the initiation of fracture along the crack front which is the reason for combining all three modes into a single parameter (eq. (14)) [47].

The c-crack behaviour which is run over by the contact path under an RCF cycle changes in a multiple stage-wise fashion as shown in Fig. 12 (a). For example, as the load reaches closer to the c-crack, the SIF  $K_I$  rises in stage 1 and then gradually decreases in stage 2 till the load reaches at the top of crack in stage 3 which results in its closure. At this instant, when the load is right at the top of c-crack, the SIF  $K_I$  becomes nil. With the advancement of load, the tensile stress linked to the rear edge of the load results in the crack tip to open up again. The SIF  $K_I$  again rises in the trailing periphery edge, however at this occasion it is low compared to the first time because of the c-crack orientation  $\phi$  (see eqs. (6)–(8) where  $\phi$  is related with both  $p_o$  and  $q(x,y)$ ).

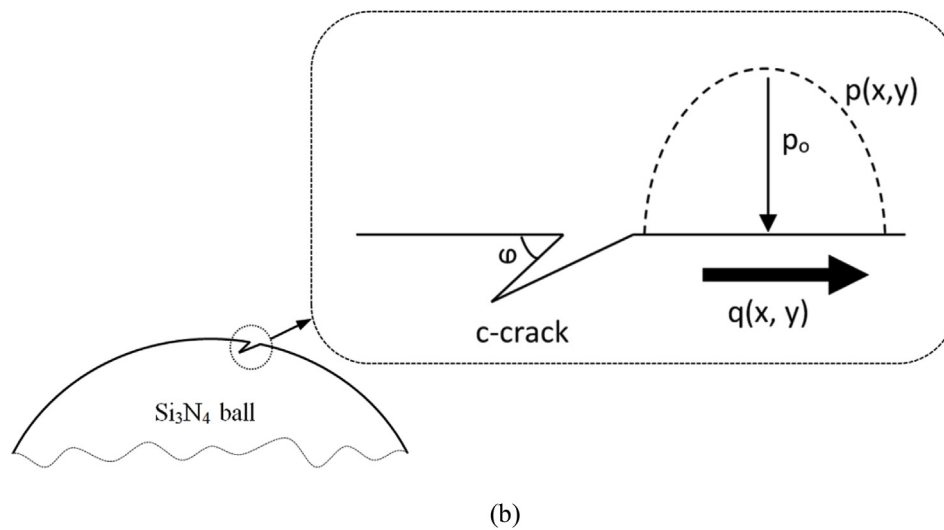
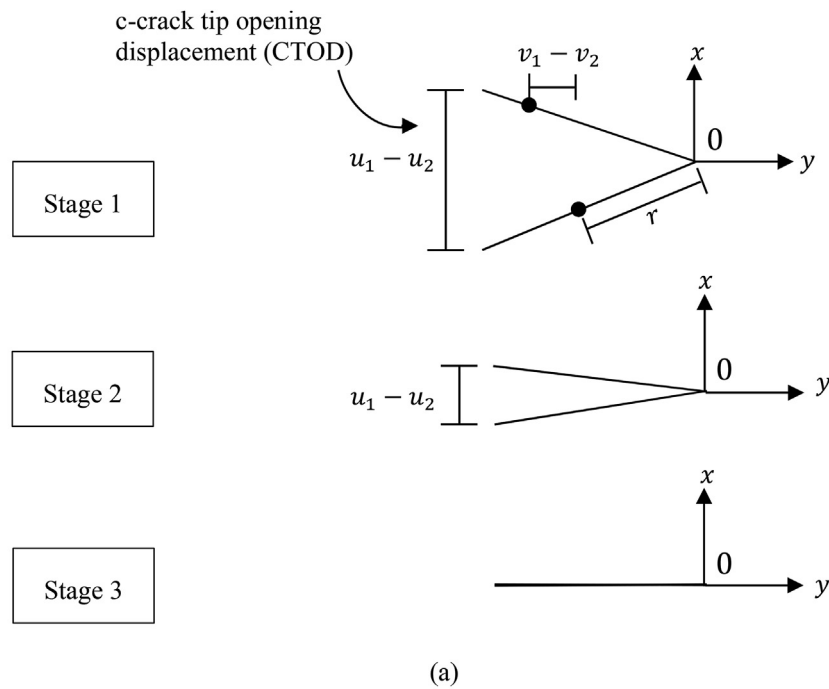


Fig. 12. (a) Schematic showing the coordinate system for the crack-tip opening displacement in stage wise fashion (b) The cross section for c-crack-tip behaviour on rolling ball with traction  $q(x, y)$  along with the maximum Hertzian contact pressure  $p_0$ .

The cross section for c-crack-tip behaviour on rolling  $Si_3N_4$  ball with traction  $q(x, y)$  (described in eqs. (6) and (7)) along with the maximum Hertzian contact pressure  $p_0$  is shown in Fig. 12 (b).

### 3.1.4. FEA of c-crack subjected to RCF

The transient state Finite element analysis (FEA) based on Abaqus 2016 was utilised to study 3D c-crack for the calculations of mixed-mode SIFs under the RCF as shown in Fig. 13. The study was performed for various positions and geometries of 3D c-cracks as functions of initial conditions (coefficient of friction and contact path size) during oblique spherical contact. The dual boundary element method (DBEM) was used to analyse the crack growth and the direction of growth. The DBEM considers two independent equations, the displacement and traction boundary integral equations, within the same integration path. The crack is characterized by two distinct elements having similar location. Every element represents the face of the crack. The displacement and traction boundary integral equations are on the surface of the

crack. As the boundary integral equations and coplanar characteristic of crack surface require continuous displacements and tractions for their existence therefore discretisation was carefully modelled.

In FEA, a small vertical semi-elliptical crack ( $a = 10 \mu m$  and  $b = 10 \mu m$ ) was inserted into a  $Si_3N_4$  block ( $E = 310 \text{ GPa}$ ,  $\nu = 0.28$ ). The tetrahedron elements was used to accurately model the stresses at the crack tip [46]. In order to extract SIFs in the surrounding area adjacent to the crack tip, it is important to maintain the constant shape of tetrahedron elements at the tip [48]. The reason for choosing tetrahedron instead of well-known hexahedral elements is the curvilinear and closed geometry of c-crack tip which makes the hexahedral elements distorted at the tip [49]. By adapting this procedure, it became possible to create a tube of tetrahedron elements around the crack tip area which therefore meshed sufficiently large region of the cracked body while maintaining the SIF accuracy.

The properly meshed area around the crack tip was loaded with an applied Hertz pressure distribution, as analysed with the stress analysis

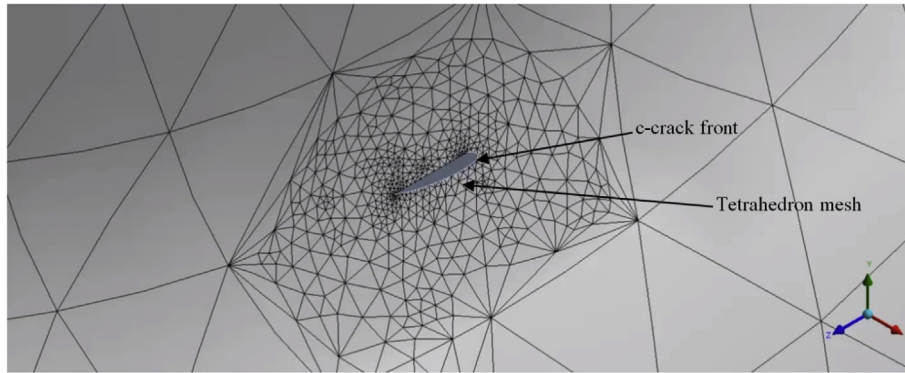


Fig. 13. FEA utilised to study the 3D c-crack for the calculations of mixed-mode SIFs under the RCF.

technique. To grow a crack using DBEM after the displaced state was calculated, SIFs for isotropic materials were calculated by the displacement correlation equations (11)–(13).

There are varieties of methods to extract the SIFs from such mesh for instance, stress matching [50] and virtual crack extension [51]. However in this paper crack tip opening displacement (CTOD) method (shown in Fig. 12 (a)) has been utilised as it is based purely on the effects of physical mechanisms without the requirement of altering its equations compared to other methods.

### 3.2. Uncertain failure probability model

This part of model (section 3.2) is based on the existing model developed by Sriram et al. [60]. The surrogate modelling and Monte Carlo Simulation here follow the existing Sriram's developed approach. This section models the uncertainty analysis for computing the RCF failure of Si<sub>3</sub>N<sub>4</sub> ball by using surrogate modelling [52,53] and Monte Carlo Simulation (MCS) [54]. Previous section uses the FEA to model the equivalent SIFs directly dependent on the crack positional, crack geometrical, loading and material properties parameters. However predicting the mean time to failure (MTTF) of Si<sub>3</sub>N<sub>4</sub> ball is a challenging task because there could be uncertainties in real operating conditions. For example, MTTF of the ball will be very large or in other words ball will not fail at-all if the c-crack is significantly small or is located outside the contact path. Therefore, RCF failure of Si<sub>3</sub>N<sub>4</sub> ball can be computed by using probabilistic approach. This section aims to compute the uncertain failure probability of Si<sub>3</sub>N<sub>4</sub> ball under operating conditions.

#### 3.2.1. Surrogate modelling

In this paper, surrogate modelling techniques such as: response surface methodology (RSM), Kriging, radial basis function (RBF) and support vector machines (SVM) [52,53] are used to synergise the input and output parameter relationship. Any of these surrogate models can be used to easily calculate the uncertainty in output variables because surrogate models benefit in very small computational cost.

The equivalent SIF  $K_{eq}$  for c-crack on Si<sub>3</sub>N<sub>4</sub> ball is characterized with positional, geometrical and loading parameters such as: the crack orientation  $\omega$ , the normalised lateral position of crack front relative to the centre of contact path  $x_D$ , the semi major axis of surface crack  $a$  and semi minor axis of surface crack  $b$  and the maximum contact pressure  $p_0$ . Therefore, functional formula is written as,

$$K_{eq} = f \left( \underbrace{x_D, \omega}_{\text{Geometrical parameters}}, \underbrace{a, b}_{\text{Positional parameters}}, \underbrace{p_0}_{\text{Loading parameter}} \right) \quad (15)$$

Though the function  $f$  in the above equation is not known however  $f$

can be calculated for the particular input parameters by using FEA. Surrogate modelling on c-crack approximates the function  $f$  by utilising straightforward mathematical analysis [53]. Surrogate modelling by using function  $f$  can be used to predict a continuous function  $f_p$  from a very small quantity of available data  $f$ . Therefore, the prediction of continuous function  $f_p$  from the limited available data  $f$  by using estimated surrogate model  $\hat{f}$  and the corresponding attached error  $\epsilon$  can be formulated as,

$$f_p = \hat{f} + \epsilon \quad (16)$$

With reference to eq. (16) and Fig. 14, surrogate modelling follows three steps: (1) Having the available limited data based on input parameters (from eqs. (15) and (2)) constructing a surrogate model  $\hat{f}$  from the available limited data  $f$  [model estimation], and (3) assessing the errors  $\epsilon$  attached to it [model appraisal] for prediction of continuous function  $f_p$ .

In this study, a simplified surrogate model is used to approximate the equivalent SIF  $K_{eq}$ , as given in eq. (15), which is a function of five parameters:  $x_D, \omega, a, b$  and  $p_0$ . Out of these five parameters, the effects of orientation ( $\omega$ ), lateral position ( $x_D$ ), semi major axis ( $a$ ), and semi minor axis ( $b$ ) are not straightforward, and thus, require approximation by using surrogate models, therefore the predicted decoupled effects of these parameters ( $x_D, \omega, a$  and  $b$ ) on the equivalent SIF  $K_{eq}$  are given as;

$$K_{eq}(\omega) = \frac{p_0}{2.5GPa} \times \frac{1}{f(\omega)} \times x_D \times \sqrt{b/a} \quad (17(a))$$

$$K_{eq}(x_D) = \frac{p_0}{2.5GPa} \times \frac{1}{\omega} \times f(x_D) \times \sqrt{b/a} \quad (17(b))$$

$$K_{eq}(b/a) = \frac{p_0}{2.5GPa} \times \frac{1}{\omega} \times x_D \times f(b/a) \quad (17(c))$$

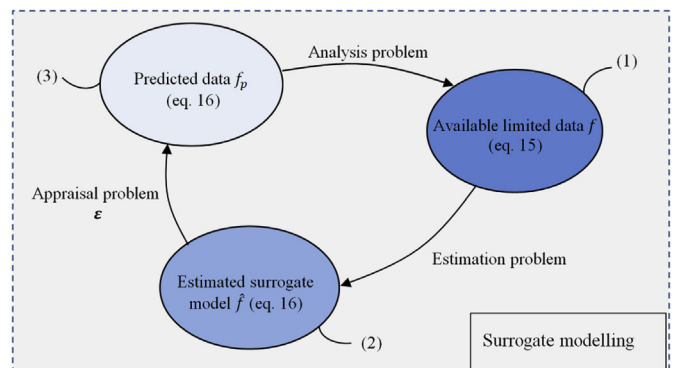


Fig. 14. Three steps of surrogate modelling for RCF study.

The equations are based on the assumption that the maximum contact pressure  $p_0$  remains constant.

The results section will show that the equivalent SIF  $K_{eq}$  values from all four surrogate models (RSM, Kriging, RBF and SVM) are very close to each other (for example Fig. 19) and it is hard to figure out the best surrogate model. Therefore for figuring out the best surrogate model, the cross-validation by using PRESS (predicted residual error sum of squares) can be used [55]. From a surrogately fitted model, every predictor  $x_i, i = 1 \dots n$  is discarded while refitting the model with  $n-1$  points. Where  $x$  indicates the input parameters  $\omega, x_D, a$  and  $b$ . The predicted value  $\widehat{K}_{eq_{i-1}}$  is computed at the discarded point  $x_i$  and the PRESS formulation is written as,

$$PRESS = \sum_{i=1}^n (K_{eq_i} - \widehat{K}_{eq_{i-1}})^2 \tag{18}$$

PRESS is a well-known method to figure out the best surrogates. Smaller PRESS value accounts for the more effective surrogate and vice versa.

### 3.2.2. Monte Carlo Simulation (MCS) using surrogate modelling

After selecting the surrogate models, the uncertainty in SIF is computed in relation to uncertainty in input parameters by using these

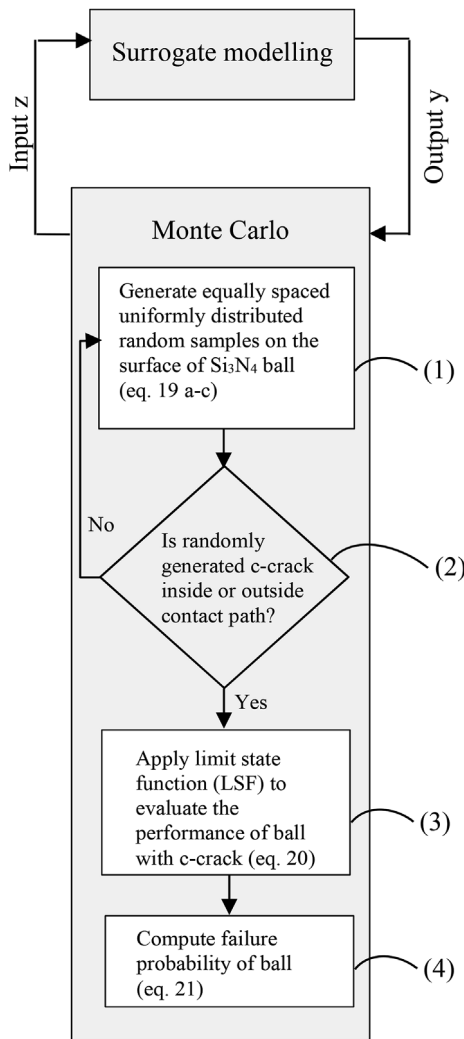


Fig. 15. Flowchart showing the steps involved in the Monte Carlo simulation. Monte Carlo works in combination with surrogate model to predict the uncertain failure probability of ball.

models. As surrogate model performs function approximation in an extremely fast manner, therefore MCS is adapted to compute failure probability by using the approximated function. The process is to use MCS for producing significant number of random samples (input  $z$ ) of input parameters as per their type of distribution. Then to apply these input samples to the surrogate model for producing output SIFs samples (output  $y$ ) according to Fig. 15. By using MCS, generating the random samples of uniformly distributed crack geometries ( $a, b$ ) and orientations  $\phi$  is quite easy however samples generation of lateral positions  $x_D$  is a difficult task as they are uniformly distributed throughout the ball sphere.

According to Fig. 15, MCS involves four steps; (1) the first step of MCS is that the surface of ball should possess equally spaced uniformly distributed random samples according to Archimedes formula as shown in Fig. 16. The Archimedes formula states that two distinct random variables which are uniformly distributed:  $\theta \in [0, 2\pi]$  and  $u \in [-1, 1]$  are sampled based on the types of their distribution [56]. Every combination of  $(\theta, u)$  indicates the random sample on the sphere. The coordinates  $(x, y, z)$  of this random sample  $(\theta, u)$  are written as;

$$x = \sqrt{1 - u^2} \cos \theta \begin{cases} \text{If } x = \left[ x_D \leq \frac{b'}{D} \right] \text{ then c-crack is inside contact path} \\ \text{If } x = \left[ x_D > \frac{b'}{D} \right] \text{ then c-crack is outside contact path} \end{cases} \tag{19(a)}$$

$$y = \sqrt{1 - u^2} \sin \theta \tag{19(b)}$$

$$z = u \tag{19(c)}$$

The next step (2) involves the condition which applies to the particular random sample that is, if  $x = \left[ x_D \leq \frac{b'}{D} \right]$  then the c-crack is inside the contact path otherwise it is outside. Where,  $D$  is the diameter of ball and  $b'$  is the semi-minor axis of the elliptical contact path. If the condition is such that c-crack is inside the contact path then eq. (17) (b) can be used to calculate the effect of  $x_D$  on equivalent SIF  $K_{eq}$ .

In the MCS, many simulations are performed. For our case in step (3), in each simulation, the values of equivalent SIF  $K_{eq}$  are randomly generated according to the above procedure and then the limit state function (LSF) is used to evaluate the performance in each simulation [57].

$$Z(t) = K_{eq} - K_{eq_{th}} \begin{cases} \text{if } Z > 0 \text{ than failure occurred} \\ \text{if } Z \leq 0 \text{ than failure not occurred} \end{cases} \tag{20}$$

Where,  $K_{eq_{th}}$  is the fatigue threshold. Lower  $K_{eq_{th}}$  accounts for high  $Z$  (failure rate) and therefore results in earlier failure due to less material toughness.

In step (4) the probability of failure  $P_f [Z > 0]$  is estimated as,

$$P_f [Z(t) > 0] = \frac{N_f}{N} \tag{21}$$

Where,  $N_f$  is the number of simulations with  $Z > 0$ , and  $N$  is the total simulation number.

Similarly, the reliability is given as,

$$R(t) = e^{-Z(t)} \tag{22}$$

Finally, the Mean Time to Failure (MTTF) of  $Si_3N_4$  ball can be calculated by utilising eqs. (20) and (21) as,

$$MTTF = \frac{1}{Z(t)} \tag{23}$$

Note that MTTF is an inverse function of both SIFs  $K_{eq}$  and  $K_{eq_{th}}$ .

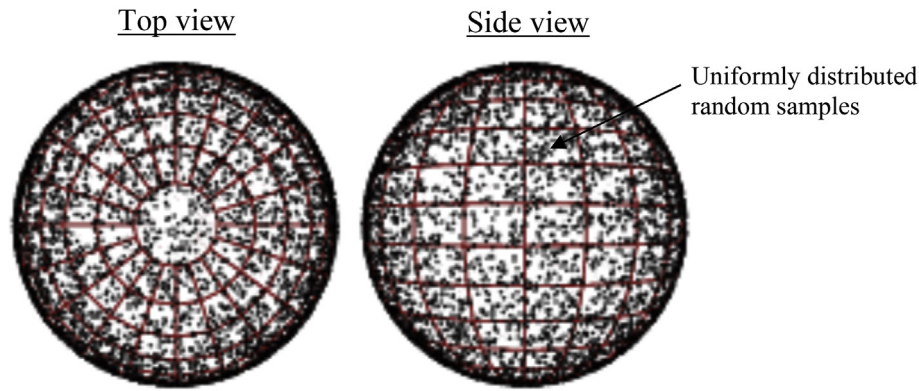


Fig. 16. The surface of ball possessing equally spaced uniformly distributed random samples.

Table 2

The distributions of input parameters for the prediction of fatigue failure probability.

Input parameter	Value	Random (R)/ Deterministic (D)
Ball diameter, $D$	12.7 mm	D
Maximum contact pressure, $p_0$	$6.23 \pm 0.5$ GPa	D
Friction coefficient, $\mu$	0.6	D
Fatigue threshold, $K_{eqth}$	[1.78–3.12 GPa $\sqrt{m}$ ]	R
Semi major length of crack, $a$	0.20–0.40 mm	R
Semi minor length of crack, $b$	0.30–0.95 mm	R
Crack orientation, $\phi$	[0 to 90°]	R
Crack position, $x_D$	Uniformly distributed on ball surface	R

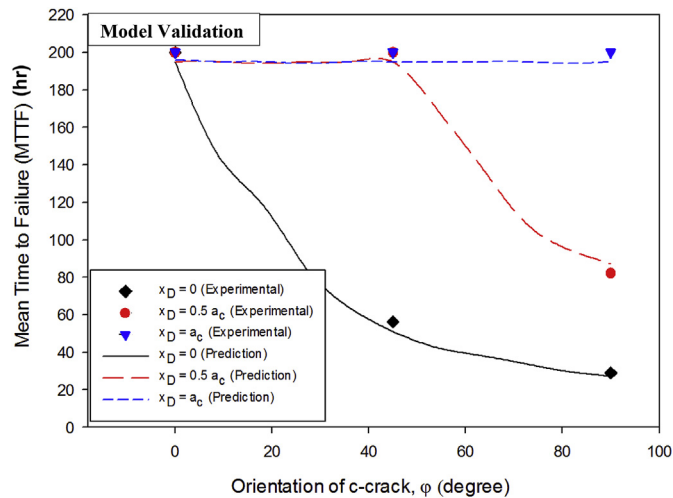


Fig. 17. The predicted results of MTTF as a function of crack orientation  $\phi$  and lateral position  $x_D$ .

#### 4. Results and discussion

Quantification of uncertainty in input parameters is the preliminary step during the analysis of uncertain prediction of fatigue failure probability. The input parameters which have been utilised in uncertainty analysis are mentioned in Table 2. It can be seen that a few parameters have been indicated as deterministic (D) while some have been indicated as random (R). In the rolling element, it is highly likely that the diameter of ball bearings will be different due to manufacturing tolerances. However, still ball diameter is treated as a deterministic

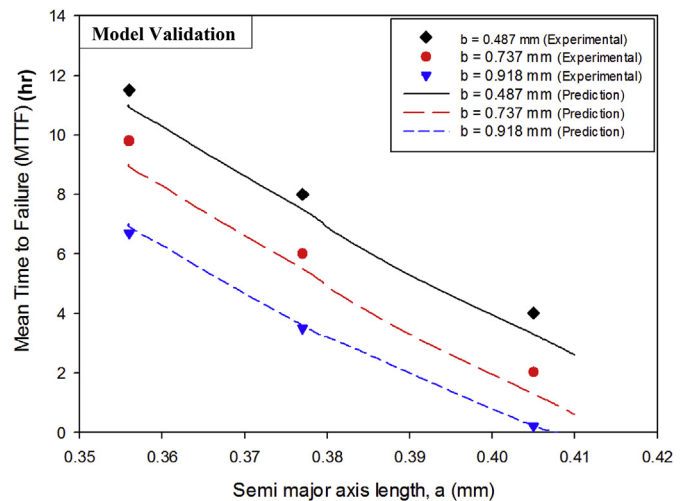


Fig. 18. The predicted results of MTTF as a function of semi major and minor axis  $a$  and  $b$  respectively.

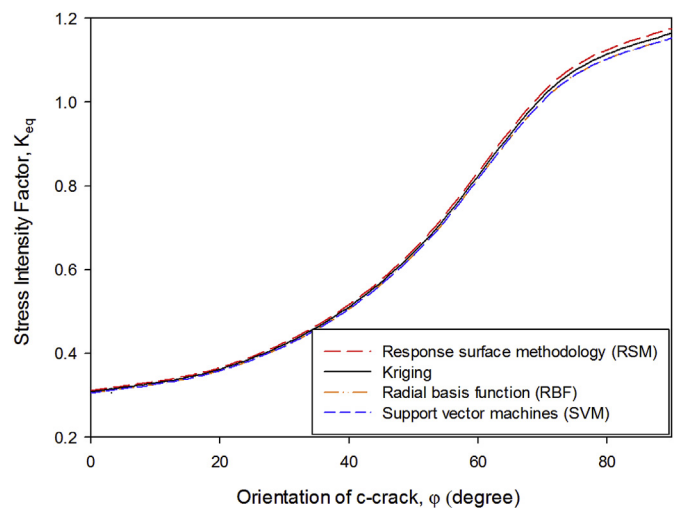


Fig. 19. Surrogate models have been utilised to study the effects of crack orientation  $\phi$  on the equivalent SIF  $K_{eq}$ .

value as the uncertainty linked to it is very small relative to others and the influence of ball diameter on RCF is minor.

It is important to validate the reliability of the developed model by using the mentioned input parameters in Table 2. For validation, the predicted results have been compared with the experimentally measured results as shown in Figs. 17 and 18. The predicted results of MTTF

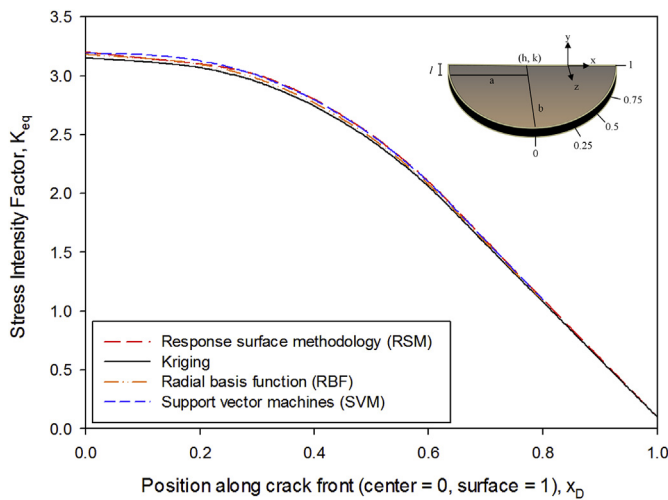


Fig. 20. Surrogate models have been utilised to study the effects of crack lateral position  $x_D$  on the equivalent SIF  $K_{eq}$ .

Table 3

Comparison of various surrogate models by using PRESS to figure out the best fitting model.

Surrogate model	$\omega$ (fig. 19)	$x_D$ (fig. 20)
RSM	0.1587	0.2105
Kriging	0.2589	0.1682
RBF	0.3189	0.2082
SVM	0.3206	0.2238

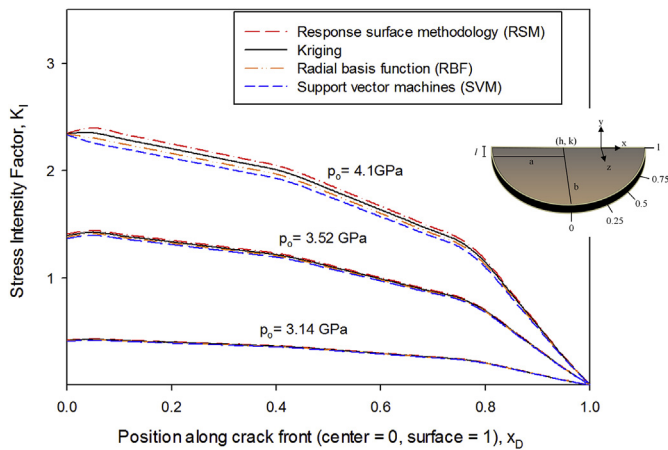


Fig. 21. The SIFs as a function of lateral position  $x_D$  for various maximum Hertzian pressure values  $p_0$ .

as a function of crack orientation  $\omega$  and lateral position  $x_D$  are shown in Fig. 17. The predicted results of MTF as a function of semi major and minor axis  $a$  and  $b$  respectively are shown in Fig. 18. Both results are in agreement with the experimental results. In the simulation, the model slightly under predicts the MTF's for some data points, which makes some points in this graph deviate from the diagonal line.

Now various surrogate models have been utilised to study the effects of crack orientation  $\omega$  and crack lateral position  $x_D$  on the equivalent SIF  $K_{eq}$ . Figs. 19 and 20 show the approximation of equivalent SIF  $K_{eq}$  for the various crack orientations  $\omega$  when  $x_D = 0$  using four different surrogate models i.e. RSM, Kriging, RBF and SVM. It should be noted that SIF  $K_{eq}$  is inversely related to MTF, as also evident from eq. (23).

It can be seen from Fig. 19 that SIF  $K_{eq}$  is lowest for  $\omega = 0^\circ$  and highest for  $\omega = 90^\circ$  confirming the results in Fig. 17 where the largest

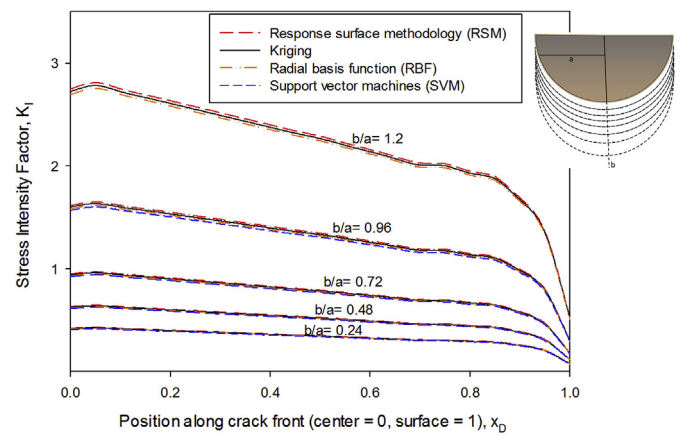


Fig. 22. The influence of elliptical shape of c-crack on the SIFs with varying aspect ratio  $b/a$ .

MTF occurs at  $\omega = 0^\circ$  and smallest MTF occurs at  $\omega = 90^\circ$ . Likewise it can be seen from Fig. 20 that SIF  $K_{eq}$  is highest for  $x_D = 0$  and lowest for  $x_D = 1$  ( $a_c$ ) confirming the results in Fig. 17 where the smallest MTF occurs at  $x_D = 0$  and highest MTF occurs at  $x_D = 1$  ( $a_c$ ).

Next the PRESS from eq. (18) is applied to the surrogated data points in Figs. 19 and 20. Table 3 mentions the PRESS values and compares them to find the best surrogate model. The results reveal that RSM is best to fit the orientation  $\omega$  (highlighted grey in Table 3) and Kriging is best to fit the lateral position  $x_D$ . PRESS analytics works according to criterion i.e. ‘smallest is the best’.

The increase in the maximum Hertzian pressure  $p_0$  results in an increase in the corresponding c-crack tip opening due to rise in SIF  $K_I$ . Most of the rolling elements have the maximum Hertzian pressure  $p_0$  within the range of 1.2–7.5 GPa [58]. Fig. 21 shows the SIF  $K_I$  as a function of lateral position  $x_D$  for various maximum Hertzian pressure values  $p_0$ . It can be seen in Fig. 21 that SIF  $K_I$  of c-crack (having semi-major axis  $a = 0.21$  mm, depth  $l = 0.075$  mm, and an orientation of  $\omega = 40^\circ$ ) increases with the increase in the maximum Hertzian pressure  $p_0$ . It can also be seen that the SIF  $K_I$  is highest along the position at the centre (0) compared to the surface (1) of the c-crack. This information can be used by others in the field with different values of pressure  $p_0$  to evaluate the SIFs based on their specific requirements.

The elliptical shape of c-crack significantly affects the corresponding c-crack tip opening due to SIF  $K_I$ . The influence of elliptical shape of c-crack on the SIF  $K_I$  with varying semi-minor axis (i.e.  $b$ ) is analysed in Fig. 22. Fig. 22 shows that as  $b/a$  aspect ratio increases from 0.24 to 1.2, the SIF  $K_I$  also increases. Also highest increase in SIF  $K_I$  is observed at the centre (0) compared to the surface (1) of the c-crack. The propagation of c-crack under RCF might result in an increase in the elliptical ratio ( $b/a$ ), especially when semi major axis remains constant. Such increase in  $b/a$  corresponding to the propagating behaviour of c-crack will result in the increase in SIF  $K_I$  along the crack front.

Now the effects of approaching load on SIFs of c-crack during RCF are analysed. The analysis of c-crack under a single RCF cycle involves many steps which are shown in Fig. 23. Fig. 23 plots the varying SIFs with normalised location ( $\frac{x_d}{a}$ ) of load on the elliptical contact path such that when  $\frac{x_d}{a} = 0$ , the load is just above the c-crack. It can be seen in figure that as the load reaches closer to the c-crack, all the SIFs ( $K_I$ ,  $K_{II}$ ,  $K_{III}$  and  $K_{eq}$ ) are highest at  $\frac{x_d}{a} = -4$ . However, as the load gradually approaches further close to the c-crack, it results in the decreasing trends of all SIFs due to crack tip closure. The c-crack tip closes completely and all the SIFs reach to the minimum level when the load is just above the crack. With the advancement of load, the tensile stress on the rear edge of the load causes the crack tip to open up again. The SIFs rise again in the trailing periphery edge, however at this occasion their level is low compared to the first time because of the c-crack orientation  $\omega$ . It

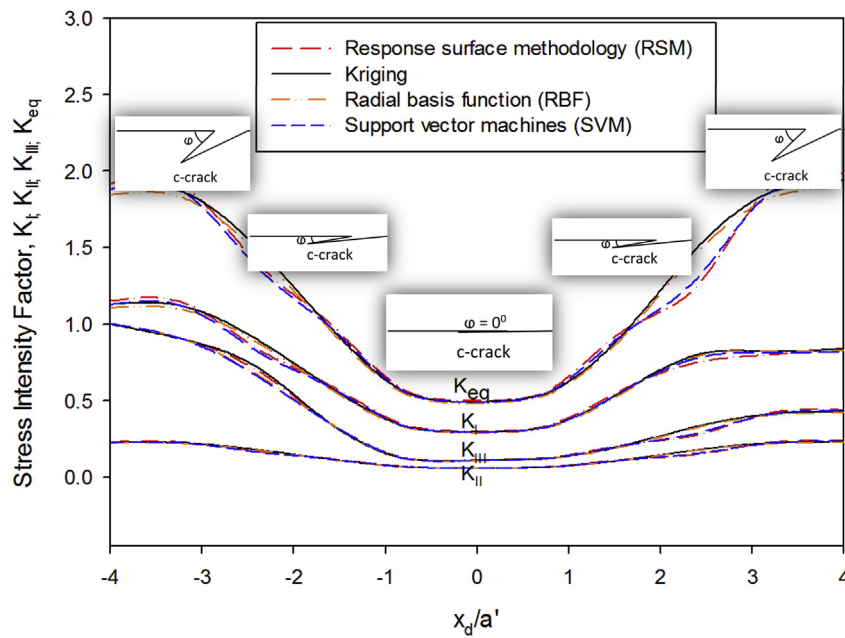


Fig. 23. The behaviour of c-crack under a single RCF cycle changing in a step wise manner.

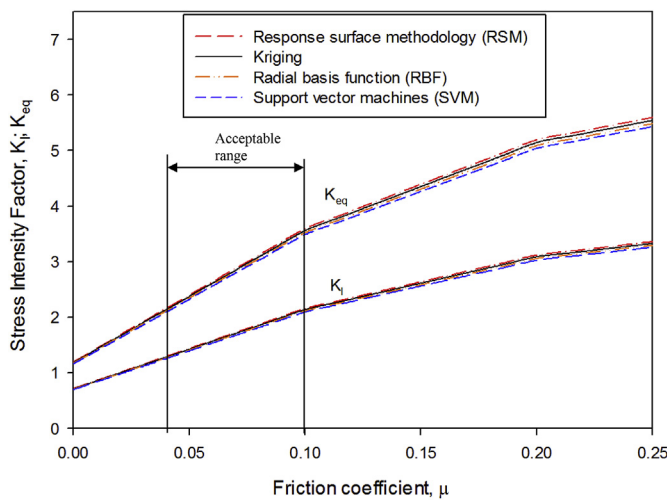


Fig. 24. The SIF  $K_I$  and SIF  $K_{eq}$  as a function of varying friction coefficient  $\mu$

can be seen from figure that both  $K_I$  and  $K_{III}$  decay and rise quickly compared to  $K_{II}$ . The reason is that both  $K_I$  (mode I crack opening) and  $K_{III}$  (Mode III Tearing) are the major fracture phenomenon observed during RCF.

The friction coefficient in bearings when subjected to elastohydrodynamic (EHD) lubrication is generally in the range of 0.04–0.10 [58]. While the value of friction coefficient seems small however the modelling results reveal that it has a major influence on the SIFs during RCF. The ball experiences both normal and traction forces induced by the contact path during RCF. As in our case the bearings are lubricated with full-slip ball-to-ball contact therefore the surface traction is negligible due to shearing properties of lubricant.

It can be seen from Fig. 24 that both SIF  $K_I$  and SIF  $K_{eq}$  increase with the increase in friction coefficient  $\mu$ . Most of the studies show that  $\mu = 0.04$  to 0.10 acts as a satisfactory range for many bearings [59]. However, beyond this range, the traction force increases which results in much steeper trends indicating large SIFs  $K_I$  and  $K_{eq}$ . The cause of SIFs getting significantly affected by the frictional coefficient is the tangential traction force which directly results in the crack opening. In

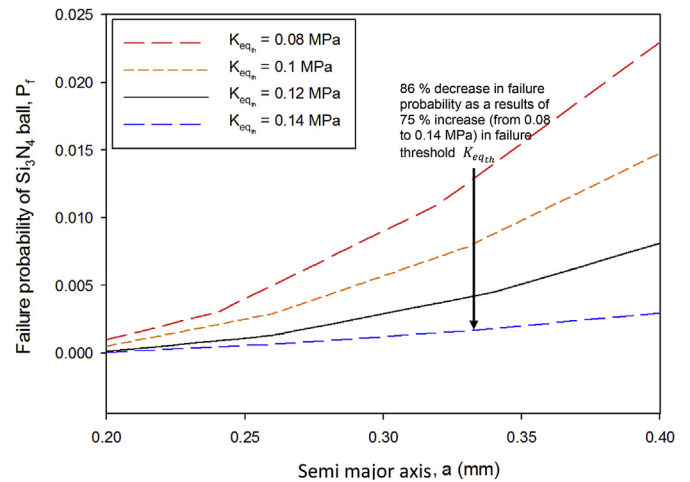


Fig. 25. The varying failure probability with changing semi major axis  $a$  of a c-crack.

addition, the large normal pressure  $p$  greatly contributes to a traction load according to eq. (2) i.e.  $g = \mu p(x, y)$  (for example, according to eq. (2), for  $p = 2.6$  GPa and  $\mu = 0.07$ , the tangential traction stress of 0.18 GPa contributes to the crack opening).

The varying failure probability with changing semi major axis  $a$  of a c-crack is shown in Fig. 25. It can be seen that the probability of failure is significantly affected by the semi major axis  $a$ . For example, for the case when fracture threshold  $K_{eq,th} = 0.08$  Mpa (red trend) and if the semi major axis  $a$  is reduced by 50% (from 0.4 to 0.2 mm) then the probability of failure  $P_f$  is decreased by 95% (from 0.023 to 0.0001). Moreover, with the increase in fracture threshold  $K_{eq,th}$  of material by 75% (0.08–0.14 MPa) the probability of failure  $P_f$  is reduced by 86%. Therefore the mutual improvements of both the semi major axis  $a$  and the fracture threshold  $K_{eq,th}$  play a vital role in improving the probability of failure  $P_f$  of  $Si_3N_4$  ball.

Similarly, the position along the crack front  $x_D$  plays a critical role in failure probability of ball as shown in Fig. 26. However, unlike the semi major axis  $a$ , it is very difficult to control the lateral position of cracks during manufacturing process as it is by nature random. It can be seen

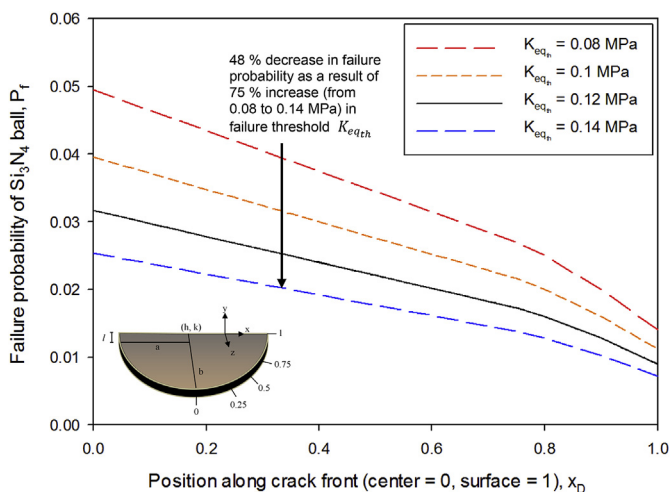


Fig. 26. The varying failure probability with position along the crack front  $x_D$  of c-crack.

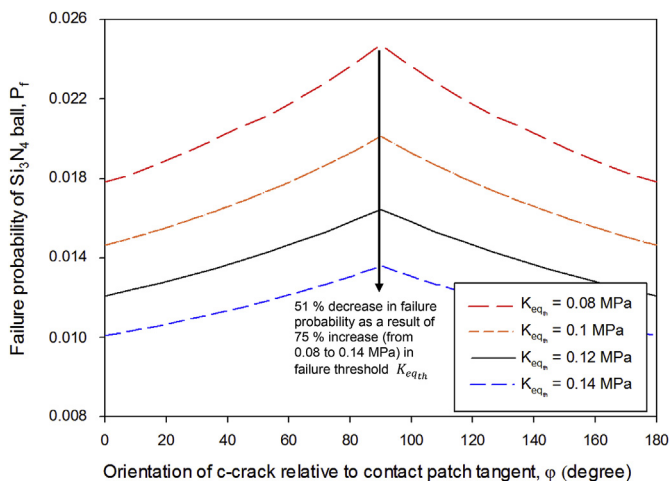


Fig. 27. The varying failure probability with orientation of c-crack  $\phi$

from Fig. 26 that for the case when fracture threshold  $K_{eqth} = 0.08$  Mpa (red trend) and if the lateral position is decreased by 100% (from 1.0 to 0.0 mm) then the probability of failure  $P_f$  is increased significantly by 250% (from 0.014 to 0.0495). Moreover, in combination with  $x_D$ , if the fracture threshold  $K_{eqth}$  of material is increased by 75% (0.08–0.14 MPa) then the probability of failure  $P_f$  is decreased by 48%.

Likewise, another input parameter i.e. orientation of crack  $\phi$  directly influences the failure probability of ball as shown in Fig. 27. Fig. 27 shows that for the case when fracture threshold  $K_{eqth} = 0.08$  Mpa (red trend) and if orientation is changed from  $0^\circ$  to  $90^\circ$  then the probability of failure  $P_f$  is increased significantly by 31% (from 0.0152 to 0.0241). Likewise decrease is seen when orientation is changed from  $90^\circ$  to  $180^\circ$ . Moreover, in combination with  $\phi$ , if the fracture threshold  $K_{eqth}$  of material is increased by 75% (0.08–0.14 MPa) then the probability of failure  $P_f$  is decreased by 51%.

Therefore from the above discussion, it can be established that the combined improvements of fracture threshold  $K_{eqth}$  and input parameters ( $a$ ,  $x_D$  and  $\phi$ ) can help to significantly improve the failure probability of ball. Figs. 25–27 can help in identifying the best material combination and non-destructive evaluation method to achieve the standard safety of bearing applications.

### 5. Conclusions

A comprehensive model has been developed for predicting the failure probability of  $Si_3N_4$  ball bearings under various uncertainties by using the combined 3D FEA with surrogate modelling and Monte Carlo simulations. The FEA generates the SIFs induced at the crack front which are then used by surrogate models and Monte Carlo simulations for estimating the uncertain propagation and the fatigue failure probability respectively. The results are relevant and of direct interest to hybrid and ceramic bearings industry.

This research concludes the subsequent points;

- The 3D FEA was conducted to evaluate the equivalent SIF  $K_{eq}$  along the crack front under RCF directly dependent on the input parameters; crack lateral position, orientation, geometry and contact pressure. These SIFs values were used by surrogate models for uncertain propagation. Finally, the Monte Carlo simulations combined with surrogate models were used to predict the failure probability of  $Si_3N_4$  ball.
- The modelling results revealed that the most effective way to reduce the failure probability of ball is by decreasing the maximum crack size and improving fracture threshold (toughness) of ball material. For instance, if the maximum crack size is reduced by 50% then the failure probability of the ball is reduced by 95%. Likewise if the fracture threshold of ball material is increased by 75% the failure probability is reduced by 86%.
- Experiments were performed to analyse the effect of various c-crack parameters on the RCF failure of  $Si_3N_4$  ball. The model predictions were compared with the experimental results to verify the reliability of the model.

### Acknowledgments

Authors would like to acknowledge both financial and in-kind support provided by Bournemouth University UK.

### References

- [1] Cundill R. Rolling element bearings into the 21st century. IMechE, seminar, London. 1990.
- [2] Hadfield M. Failure of silicon nitride rolling elements with ring crack defects. *Ceram Int* 1998;24:379–86.
- [3] Khan ZA, Hadfield M. Manufacturing induced residual stress influence on the rolling contact fatigue life performance of lubricated silicon nitride bearing materials. *Mater Des* 2007;28:2688–93.
- [4] Khan ZA, Hadfield M, Tobe S, Wang Y. Ceramic rolling elements with ring crack defects—a residual stress approach. *Mater Sci Eng, A* 2005;404:221–6.
- [5] Khan ZA, Hadfield M, Tobe S, Wang Y. Residual stress variations during rolling contact fatigue of refrigerant lubricated silicon nitride bearing elements. *Ceram Int* 2006;32:751–4.
- [6] Khan ZA, Hadfield M, Wang Y. "Pressurised chamber design for conducting rolling contact experiments with liquid refrigerant lubrication. *Mater Des* 2005;26:680–9.
- [7] Wang Y, Hadfield M. A study of line defect fatigue failure of ceramic rolling elements in rolling contact. *Wear* 2002;253:975–85.
- [8] Wang Y, Hadfield M. The influence of ring crack location on the rolling contact fatigue failure of lubricated silicon nitride: experimental studies. *Wear* 2000;243:157–66.
- [9] Wang Y, Hadfield M. Life prediction for surface crack initiated contact fatigue of silicon nitride bearing balls. *Tribology series*, vol. 41. Elsevier; 2003. p. 349–58.
- [10] Wang Y, Hadfield M. Failure modes of ceramic rolling elements with surface crack defects. *Wear* 2004;256:208–19.
- [11] Wang Y, Hadfield M. A mechanism for nucleating secondary fractures near a pre-existing flaw subjected to contact loading. *Wear* 2003;254:597–605.
- [12] Wang Y, Hadfield M. The influence of ring crack location on the rolling contact fatigue failure of lubricated silicon nitride: fracture mechanics analysis. *Wear* 2000;243:167–74.
- [13] Levesque GA, Arakere NK. Critical flaw size in silicon nitride ball bearings. *Tribol Trans* 2010;53:511–9.
- [14] Levesque G, Arakere NK. An investigation of partial cone cracks in silicon nitride

- balls. *Int J Solid Struct* 2008;45:6301–15.
- [15] Sadeghi F, Jalalahmadi B, Slack TS, Raje N, Arakere NK. "A review of rolling contact fatigue. *J Tribol* 2009;131:041403.
- [16] Melchers RE, Beck AT. *Structural reliability analysis and prediction*. John Wiley & Sons; 2017.
- [17] Tu J, Choi KK, Park YH. A new study on reliability-based design optimization. *J Mech Des* 1999;121:557–64.
- [18] Qu X, Haftka R. Reliability-based design optimization using probabilistic sufficiency factor. *Struct Multidiscip Optim* 2004;27:314–25.
- [19] Nazir MH, Khan ZA, Saeed A, Stokes K. Modeling the effect of residual and diffusion-induced stresses on corrosion at the interface of coating and substrate. *Corrosion* 2015;72:500–17. 2016/04/01.
- [20] Nazir MH, Khan ZA, Saeed A, Stokes K. A predictive model for life assessment of automotive exhaust mufflers subject to internal corrosion failure due to exhaust gas condensation. *Eng Fail Anal* 2016;63:43–60.
- [21] Nazir MH, Khan ZA, Stokes K. A holistic mathematical modelling and simulation for cathodic delamination mechanism – a novel and an efficient approach. *J Adhes Sci Technol* 2015:1–39.
- [22] Nazir MH, Khan Z, Stokes K. Modelling of metal-coating delamination incorporating variable environmental parameters. *J Adhes Sci Technol* 2014;29:392–423.
- [23] Nazir M, Khan Z, Saeed A, Stokes K. Modelling the effect of residual and diffusion induced stresses on corrosion at the interface of coating and substrate. *Corrosion* 2015;72(4).
- [24] Nazir MH, Khan ZA, Stokes K. Optimisation of interface roughness and coating thickness to maximise coating-substrate adhesion - a failure prediction and reliability assessment modelling. *J Adhes Sci Technol* 2015;29:1415–45.
- [25] Saeed A, Khan ZA, Nazir MH. Time dependent surface corrosion analysis and modelling of automotive steel under a simplistic model of variations in environmental parameters. *Mater Chem Phys* 8/1/2016;178:65–73.
- [26] Nazir M, Khan ZA, Stokes K. A unified mathematical modelling and simulation for cathodic blistering mechanism incorporating diffusion and fracture mechanics concepts. *J Adhes Sci Technol* 2015;29:1200–28.
- [27] Nazir MH, Khan ZA, Stokes K. Analysing the coupled effects of compressive and diffusion induced stresses on the nucleation and propagation of circular coating blisters in the presence of micro-cracks. *Eng Fail Anal* 2016;70:1–15.
- [28] Nazir MH, Saeed A, Khan Z. "A comprehensive predictive corrosion model incorporating varying environmental gas pollutants applied to wider steel applications. *Mater Chem Phys* 2017;193:19–34.
- [29] Nazir M, Khan Z. A review of theoretical analysis techniques for cracking and corrosive degradation of film-substrate systems. *Eng Fail Anal* 2016;72:80–113.
- [30] Bajwa R, Khan Z, Nazir H, Chacko V, Saeed A. Wear and friction properties of electrodeposited Ni-Based coatings subject to nano-enhanced lubricant and composite coating. *Acta Metallurgica Sin* 2016;29:902–10.
- [31] Nazir MH, Khan Z. Maximising the interfacial toughness of thin coatings and substrate through optimisation of defined parameters. *J Int Comput Meth Exp Meas* 2015;3:316–28.
- [32] Bajwa RS, Khan Z, Bakolas V, Braun W. Effect of bath ionic strength on adhesion and tribological properties of pure nickel and Ni-based nanocomposite coatings. *J Adhes Sci Technol* 2016;30:653–65.
- [33] Bajwa RS, Khan Z, Bakolas V, Braun W. Water-lubricated Ni-Based composite (Ni–Al<sub>2</sub>O<sub>3</sub>, Ni–SiC and Ni–ZrO<sub>2</sub>) thin film coatings for industrial applications. *Acta Metallurgica Sin* 2015;29:8–16.
- [34] M. H. Nazir, Z. A. Khan, A. Saeed, A. Siddaiah, and P. L. Menezes, "Synergistic wear-corrosion analysis and modelling of nanocomposite coatings," *Tribol Int*, vol. 121, pp. 30–44, 2018/05/01/2018.
- [35] Nazir MH, Khan ZA, Saeed A, Bakolas V, Braun W, Bajwa R, Rafique S. Analyzing and modelling the corrosion behavior of Ni/Al<sub>2</sub>O<sub>3</sub>, Ni/SiC, Ni/ZrO<sub>2</sub> and Ni/Graphene nanocomposite coatings. *Materials* 2017;10:1225.
- [36] Khan ZA, Latif J, Nazir H, Saeed A, Stokes K. Predictive and prognostic modelling and simulation of coating failures due to corrosion and mechanical failures. *J Int Comput Meth Exp Meas* 2018;6:487–98.
- [37] Latif J, Khan ZA, Nazir MH, Stokes K, Plummer J. Life assessment prognostic modelling for multi-layered coating systems using a multidisciplinary approach. *Mater Sci Technol* 2017:1–15.
- [38] Nazir MH, Khan ZA, Saeed A. A novel non-destructive sensing technology for on-site corrosion failure evaluation of coatings. *IEEE Access* 2018;6:1042–54.
- [39] Khan ZA. *Rolling contact wear of hybrid ceramic bearings with refrigerant lubrication*. Bournemouth University; 2006.
- [40] Johnson K. *Contact mechanics*. Cambridge: Cambridge University Press; 1985. UK.
- [41] Wang Y, Hadfield M. Rolling contact fatigue failure modes of lubricated silicon nitride in relation to ring crack defects. *Wear* 1999;225:1284–92.
- [42] Johnson K. "Contact mechanics. Cambridge: Cambridge Univ," Press; 1985.
- [43] Burke J, Gorum A, Katz R. "Ceramics for high performance applications. Massachusetts: Brook Hill Publ," Co; 1974. p. 15.
- [44] Paulson NR, Sadeghi F, Habchi W. A coupled finite element EHL and continuum damage mechanics model for rolling contact fatigue. *Tribol Int* 2017;107:173–83.
- [45] Sutton MA, Deng X, Ma F, Newman Jr. JC, James M. Development and application of a crack tip opening displacement-based mixed mode fracture criterion. *Int J Solid Struct* 2000;37:3591–618.
- [46] Anderson TL. *Fracture mechanics: fundamentals and applications*. CRC press; 2017.
- [47] Bogdański S, Trajer M. "A dimensionless multi-size finite element model of a rolling contact fatigue crack. *Wear* 2005;258:1265–72.
- [48] Rajaram H, Socrate S, Parks D. Application of domain integral methods using tetrahedral elements to the determination of stress intensity factors. *Eng Fract Mech* 2000;66:455–82.
- [49] Newman J, Raju I. An empirical stress-intensity factor equation for the surface crack. *Eng Fract Mech* 1981;15:185–92.
- [50] Gu P, Dao M, Asaro R. A simplified method for calculating the crack-tip field of functionally graded materials using the domain integral. *J Appl Mech* 1999;66:101–8.
- [51] Hellen T. On the method of virtual crack extensions. *Int J Numer Meth Eng* 1975;9:187–207.
- [52] Forrester AI, Söbester A, Keane AJ. Multi-fidelity optimization via surrogate modelling. *Proceedings of the royal society of london a: mathematical, physical and engineering sciences*. 2007. p. 3251–69.
- [53] Queipo NV, Haftka RT, Shyy W, Goel T, Vaidyanathan R, Tucker PK. Surrogate-based analysis and optimization. *Prog Aero Sci* 2005;41:1–28.
- [54] Meakin P. Models for material failure and deformation. *Science* 1991;252:226–34.
- [55] Geladi P, Kowalski BR. Partial least-squares regression: a tutorial. *Anal Chim Acta* 1986;185:1–17.
- [56] Shao M-Z, Badler N. "Spherical sampling by archimedes' theorem. *Tech Rep(CIS)* 1996:184.
- [57] Li H-S, Zhao A-L, Tee KF. Structural reliability analysis of multiple limit state functions using multi-input multi-output support vector machine. *Adv Mech Eng* 2016;8. 1687814016671447.
- [58] M. M. Khonsari and E. R. Booser, "Friction and elastohydrodynamic lubrication," *Applied tribology: bearing design and lubrication: bearing design and lubrication*, pp.529–569.
- [59] Wang L, Snidle R, Gu L. Rolling contact silicon nitride bearing technology: a review of recent research. *Wear* 2000;246:159–73.
- [60] Sriram P, Levesque G, Kim NH, Arakere NK. Uncertainty analysis for rolling contact fatigue failure probability of silicon nitride ball bearings. *Int. J. Solid Struct*. September 2010;47(18–19):2543–53.